International Journal of Nanomedicine

Dovepress
Taylor & Francis Group

Open Access Full Text Article

ORIGINAL RESEARCH

Mitochondria-Targeting Virus-Like Gold Nanoparticles Enhance Chemophototherapeutic Efficacy Against Pancreatic Cancer in a Xenograft Mouse Model

Youshuai Meng[1,*], Chuan Chen[1,2,*], Ronggui Lin[1,3,*], Linlin Zheng[4], Yanying Fan[5], Mengdi Zhang[1], Ziqi Zhang[1], Han Shi[1,3], Xiaohan Zheng[1,3], Junyu Chen[1], Dezhao Chen[1,3], Tianhong Teng[1,3], Bing Chen[1]

[1]Key Laboratory of Nanomedical Technology (Education Department of Fujian Province), Department of Pharmaceutical Analysis, School of Pharmacy, Fujian Medical University, Fuzhou, 350122, People's Republic of China; [2]Innovation Center for Enzyme Catalysis and Drug Synthesis, School of Pharmacy, Xiamen Medical College, Xiamen, 361023, People's Republic of China; [3]Department of General Surgery/ Department of Obstetrics & Gynecology, Fujian Medical University Union Hospital, Fuzhou, 350001, People's Republic of China; [4]Department of Oncology, Affiliated Hospital of Putian University, Putian, 351199, People's Republic of China; [5]Fuzhou Children's Hospital of Fujian Province, Fuzhou, 350005, People's Republic of China

*These authors contributed equally to this work

Correspondence: Bing Chen, School of Pharmacy, Fujian Medical University, Fuzhou, 350122, People's Republic of China, Email BingChen_001@126.com, BingChen_001@fjmu.edu.cn; Tianhong Teng, Fujian Medical University Union Hospital, Fujian Medical University, Fuzhou, 350122, People's Republic of China, Email tianhongteng24@fjmu.edu.cn

Background: The dense and fibrotic nature of the pancreatic tumor microenvironment significantly contributes to tumor invasion and metastasis. This challenging environment acts as a formidable barrier, hindering effective drug penetration and delivery, which ultimately limits the efficacy of conventional cancer treatments. Gold nanoparticles (AuNPs) have emerged as promising nanocarriers to overcome the extracellular matrix barrier; however, their limited targeting precision, poor delivery efficiency, and insufficient photothermal conversion present challenges.

Methods: We developed triphenyl phosphonium-functionalized high-branch gold nanoparticles, denoted as Dox@TPAu, to enhance drug delivery and targeting capabilities. The targeted penetration, biopharmaceutical and pharmacokinetic properties of Dox@TPAu were characterized, and the synergistic therapeutic effect was evaluated by the BxPC-3 xenograft tumor mouse model.

Results: Dox@TPAu exhibits superior photothermal conversion efficiency (91.0%) alongside a high drug loading efficiency (26%) and effective photo-triggered drug-release potential. This Dox@TPAu drug delivery system adeptly accumulates at tumor sites due to its unique properties, enabling targeted localization within cancer cells and the mitochondria of stromal fibroblasts. This localization disrupts mitochondrial function and transfer—processes crucial for energy production, metabolism, and cell signaling within the tumor microenvironment. Pharmacokinetic analyses revealed an optimal spatiotemporal distribution of Dox@TPAu at the tumor site. This strategic accumulation enables precise disruption of both the physical barrier and cancer cells, enhancing treatment efficacy through near-infrared light-triggered local chemo-photothermal synergistic therapy.

Conclusion: Our findings demonstrate that this innovative strategy effectively leverages the unique properties of mitochondria-targeting, virus-like AuNPs for precise and efficient stromal depletion, presenting a promising approach to enhance the efficacy of pancreatic cancer treatment.

Keywords: mitochondria-targeting, gold nanoparticle, stromal depletion, chemo-photothermal therapy, pancreatic cancer

Introduction

Pancreatic cancer is one of the deadliest solid malignancies worldwide and is distinguished by its aggressive behavior and dismal prognosis. The 5-year survival rate of patients with this condition hovers around a bleak 10%.[1] Clinically,

Received: 15 October 2024
Accepted: 22 December 2024
Published: 28 December 2024

pancreatic cancer is characterized by nonspecific symptoms and reliable detection biomarkers, and more than 80% of patients present with regional or distant metastasis, resulting in missed opportunities for surgical intervention.[2] Currently, systemic therapy remains the primary treatment approach for patients with pancreatic cancer at different clinical stages; however, its overall benefits are limited.[3] The main reasons for the failure of pancreatic cancer treatment are fibrotic and stromal microenvironments, which are crucial in tumor progression and therapeutic resistance.[4] The pancreatic tumor microenvironment surrounding tumor cells exhibits myriads of complex features, such as the presence of cancer-associated fibroblasts (CAFs), mesenchymal cells, extracellular matrix (ECM), and other key components, which create a complex milieu that supports tumor cell invasion and metastasis.[5] The ECM acts as a physical barrier that impedes the delivery of chemotherapy and immunotherapy agents to the tumor microenvironment, whereas CAFs contribute to treatment resistance through the secretion of growth factors and cytokines.[6] Additionally, the tumor microenvironment plays crucial roles in both primary and acquired resistance to a range of therapies, including traditional cytotoxic chemotherapies, targeted therapies, and immune-modulating treatments.[7,8]

Accumulating evidence has demonstrated that mitochondria not only provide essential energy for cells but also play a key role in signaling pathways that affect cell survival, proliferation, and metabolism.[9,10] Recent studies have revealed that pancreatic cancer cells can transfer functional mitochondria to stromal fibroblasts through a process known as mitochondrial transfer.[11] Crosstalk between cancer cells and CAFs occurs through mitochondrial signaling pathways, inducing metabolic reprogramming, growth factor secretion, and mitochondrial DNA fusion/fission dynamics, which further promote tumor progression, metastasis, and treatment resistance.[12,13] Understanding the intricate interplay between mitochondrial structure, function, and therapeutic responsiveness in both cancer cells and stromal fibroblasts is essential for developing effective treatment strategies for pancreatic cancer.[14,15] Targeting mitochondrial dysfunction presents a promising therapeutic avenue. By specifically addressing mitochondrial damage in both pancreatic cancer cells and CAFs, we can potentially disrupt tumor growth and enhance the sensitivity of these cells to chemotherapy.[16,17] However, achieving effective delivery of mitochondria-targeted therapies poses significant challenges due to the intricate tumor microenvironment, characterized by physical barriers, heterogeneous cell populations, and vasculature.[18,19] Given the multifaceted nature of pancreatic cancer and the dynamic interplay between cancer cells and stromal fibroblasts, combination therapies targeting multiple pathways, including mitochondrial dysfunction, may be more effective than single-agent approaches.[20]

Hyperthermia therapy can substantially improve the outcomes of traditional chemotherapy and radiation therapy, and both clinical and preclinical data indicate that it will play a crucial role in future cancer treatments.[21,22] The current clinical and preclinical status of hyperthermia therapy shows promising advancements, with FDA-approved indocyanine green (ICG) and gold nanoparticles (AuNPs) demonstrating excellent biocompatibility, making this approach a feasible and effective treatment modality.[23,24] However, the use of free ICG is limited by its rapid clearance, restricted tumor accumulation, and shallow tissue penetration depth. Here, virus-like hyperbranched AuNPs offer a compelling solution due to their ability to be engineered to enhance targeting specificity to tissues or cellular organelles. This targeted approach maximizes therapeutic efficacy while minimizing systemic toxicity.[25,26] Furthermore, their unique structural features, including a high specific surface area and tunable surface chemistry, enable versatile applications in combination therapies.[27,28] Moreover, hyperbranched AuNPs possess exceptional photothermal properties, allowing them to convert absorbed radiation into heat effectively.[29,30] This capability is particularly advantageous for synergistic chemo-photothermal therapy (PTT), which can overcome drug resistance and improve overall treatment outcomes. In summary, a deeper exploration of the mechanisms by which mitochondrial targeting and virus-like AuNPs can enhance treatment efficacy is warranted. This approach not only addresses the multifaceted nature of pancreatic cancer but also leverages the interplay between cancer cells and stromal components to develop more effective combination therapies.[31,32]

In this work, we developed a novel mitochondria-targeting and synergistic therapeutic gold-based drug delivery system, referred to as Dox@TPAu, designed to overcome treatment resistance in pancreatic cancer.[33] Dox@TPAu is composed of virus-like AuNPs functionalized with triphenylphosphonium (TPP) and loaded with doxorubicin (Dox), a broad-spectrum chemotherapy drug that achieves mitochondria-specific PTT and targeted drug release, thereby facilitating precise spatiotemporal synchronization of chemotherapy and PTT. We propose that Dox@TPAu can effectively accumulate at tumor sites and maintain therapeutic concentrations by subsequently entering tumors and their

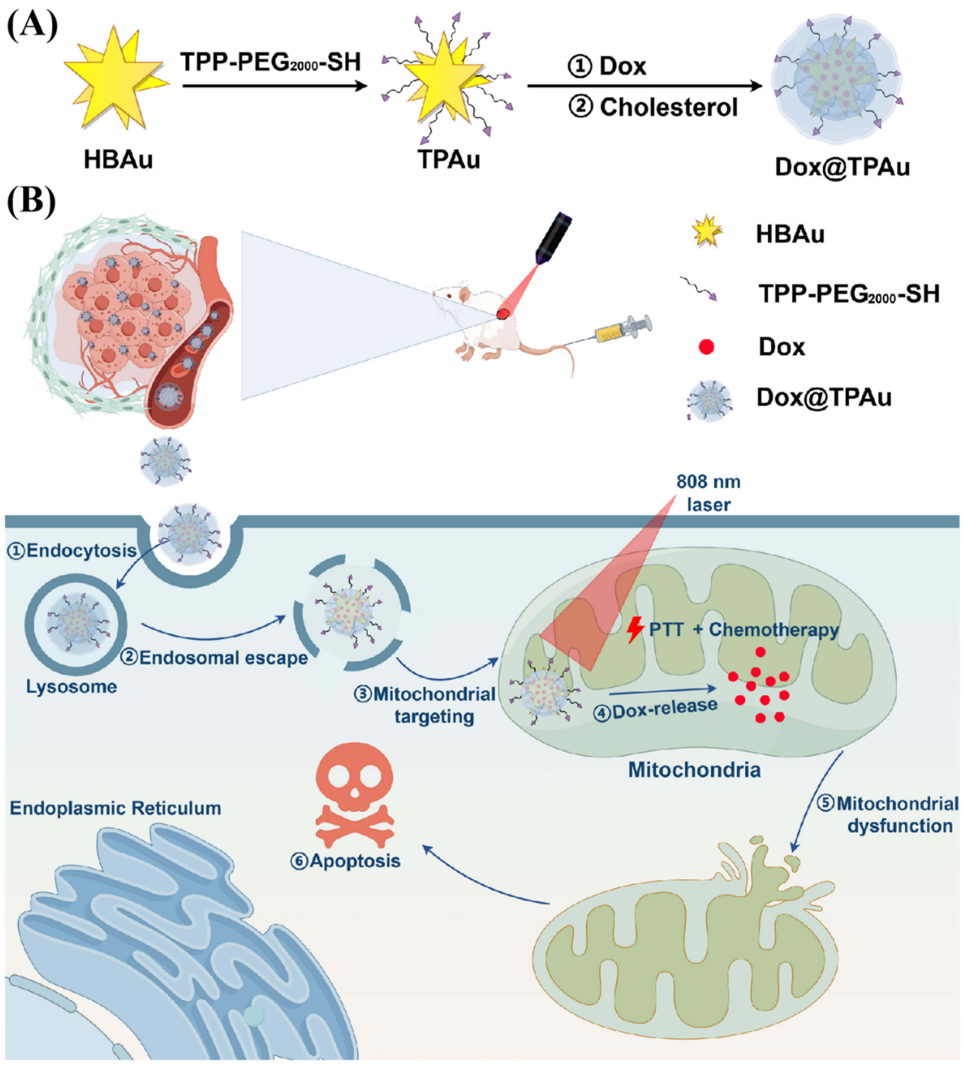

Scheme 1 Schematic diagram of photo-triggered high-branch Au nanoparticles (HBAu) via functional modification for mitochondria-targeted drug delivery. (**A**) The design and Preparation of Dox@TPAu. Dox@TPAu is composed of TPP-functionalized HBAu encapsulating Dox. (**B**) Anticancer mechanism of Dox@TPAu augmented chemophototherapeutic efficacy. Enhanced synergistic therapy relies on loosened extracellular matrix (ECM) and therapeutic sensitization due to in-situ hyperthermia therapy and drug release triggered by near-infrared (NIR) irradiation.

associated cell mitochondria. This mechanism allows Dox@TPAu to escape lysosomal degradation, harnessing the localized mitochondria-targeting ability of TPAu to enable synergistic chemo-PTT that depletes the extracellular matrix (ECM) and mitigates treatment resistance (Scheme 1). Our mitochondria-targeting virus-like AuNPs showed excellent PTT together with high and efficient drug loading for near-infrared light-triggered synergistic therapy at the cellular and organism levels.[34] Overall, this study not only realizes the design of virus-like AuNPs for mitochondria-targeting and remote photo-triggered chemo-PTT for cancer treatment but also provides a promising therapeutic strategy to amplify stromal depletion against pancreatic cancer. Furthermore, this research opens new avenues for the development of similar targeted therapies across various solid tumors that exhibit stromal barriers to drug delivery. The combination of targeted drug delivery with remotely activated therapeutic modalities holds great promise for refining cancer treatment protocols, ultimately leading to better patient outcomes.

Materials and Methods

Sodium borohydride ($NaBH_4$) and potassium iodide (KI) were purchased from Aladdin (Shanghai, China). Tetrachloroauric acid ($HAuCl_4$), trisodium citrate dihydrate (TSC), l-ascorbic acid (AA), polyvinylpyrrolidone (PVP), dopamine, and doxorubicin hydrochloride (Dox·HCl) were obtained from MedChemExpress (NJ, USA). Cholesterol and $mPEG_{2000}$-SH

https://doi.org/10.2147/IJN.S497346

were acquired from AVT Pharmaceutical Technology Co., Ltd. (Shanghai, China). TPP-PEG_{2000}-SH was obtained from Qiyue Biology (Xi'an, China). RPMI-1640 and trypsin were acquired from HyClone (Logan, UT, USA). Phosphate buffered saline (PBS) and fetal bovine serum were obtained from Herui Biotechnology (Fujian, China). MTT, calcein/PzI cell viability, and JC-1 mitochondrial potential sensor detection kits were acquired from Thermo Fisher Scientific (Waltham, MA, USA). Hoechst 33342 and MitoTracker@Red were purchased from Beyotime Biotechnology (Shanghai, China). All other chemical reagents were obtained from Sinopharm Chemical Reagent Corporation (Shanghai, China).

The in-vitro and in-vivo Studies Using Animal Model

Human pancreatic cancer cell line BxPC-3 was acquired from MeisenCTCC Cell Technology Co., Ltd. (Zhejiang, China); the cells were grown in RPMI-1640 medium supplemented with penicillin/streptomycin (1%, w/v) and 10% FBA. All cells were cultured under standard conditions in a humidified atmosphere with 5% CO_2 at 37°C.

BALB/c nude mice (male, 6–8 weeks old) were obtained from SLAC Laboratory Animal Co., Ltd. (Shanghai, China), housed in a pathogen-free controlled environment with a humidity of 50% ± 10% and an ambient temperature of 25°C ± 5°C, and provided ad libitum access to water and food under a 12-:12-h light/dark cycle. All animal experiments were performed in compliance with the Guidelines for the Care and Use Ethics Committee of Fujian Medical University (Certificate number: FJMU IACUC 2021-NSFC-0022).

Synthesis of HBAu

The synthesis of HBAu involves two main steps: first, the preparation of gold nanoseeds, followed by the formation of HBAu nanoparticles. Gold nanoseeds were prepared using a one-step seed growth method.[35] Briefly, 0.5 mL of 5 mm $HAuCl_4$ and 0.5 mL of 5 mm TSC were added into 9 mL deionized water; then, 0.3 mL of 0.1 M $NaBH_4$ was injected into the reaction solution under vigorous stirring. The solution turned yellowish-red immediately. After 5 h, 1.25 mL of 0.1 M AA, 1.25 mL of 25.4 mm $HAuCl_4$, 1 mL of 0.2 M KI, and 2.5 mL of 5 wt% PVP were added to the mixture under vigorous stirring. The gold nanoseeds were washed twice with deionized water and purified by centrifuging at 10,000 rpm for 10 min. Finally, the obtained gold nanoseeds were redispersed in deionized water at 4°C for further use.

Subsequently, 100 μL of 25.4 mm $HAuCl_4$ and 50 μL of 4 mg/mL dopamine were injected into the dispersed 100 μL of 14 nm gold nanoseed solution in 9 mL Tris-HCl buffer solution under the protection of nitrogen. The solution's color changed immediately to pale yellow and gradually darkened to black. The reactor was stirred continuously for 6 h. The HBAu nanoparticles were washed twice with deionized water and purified by centrifuging at 10,000 rpm for 10 min. Finally, the obtained HBAu nanoparticles were redispersed in deionized water at 4°C for further use.

Preparation of Dox@HBAu and Dox@TPAu

HBAu (0.1 mg/mL, 5 mL) was obtained through centrifugation, and then modified with mPEG_{2000}-SH (3 mg/mL, 5 mL) to improve its stability in a physiological environment. The modification utilizes thiol groups that form gold-sulfur bonds with the gold nanoparticle surface, effectively improving the particle's biocompatibility and longevity in biological systems. After removing the supernatant, an equal-mass aqueous solution of Dox and a cholesterol aqueous solution (4 mg/mL, 5 mL) were added, and the mixture was vigorously stirred overnight for drug loading. This facilitates the encapsulation of Dox within the hydrophobic core formed by the cholesterol, promoting effective loading onto the nanoparticles. Dox@HBAu were washed twice with deionized water to remove any unencapsulated Dox, purified by centrifuging at 12,000 rpm for 10 min, and then stored in deionized water at 4°C for further use.

The preparation protocol for Dox@TPAu was similar to that for Dox@HBAu, except that TPP-PEG_{2000}-SH was used instead of mPEG_{2000}-SH. TPP (triphenylphosphine) serves as a mitochondrial targeting moiety, allowing for specific interaction with mitochondrial membranes. Upon synthesis, the obtained Dox@TPAu were redispersed in deionized water and stored at 4°C for further use.

Characterization of Dox@TPAu

The mean hydrodynamic diameter, polydispersity index, and zeta potential of the gold nanoseeds and Dox@TPAu were analyzed using a dynamic laser light scattering (DLS) system (Anton Paar, USA). The UV-Vis and near-infrared light

(NIR) absorption spectra of HBAu were recorded in the range for 400–900 nm using a UV-2600 spectrophotometer (Shimadzu, Japan). The Dox content in the AuNPs and biological samples was determined using an HPLC-MS/MS system (Agilent, USA) that was equipped with a ChromCore C18 column (150 mm × 4.6 mm, 5 μm; Welch Materials, Inc., Ellicott, MD, USA). Encapsulated and free drugs were separated through high-speed centrifugation, allowing for the assessment of encapsulation efficiency and drug loading capacity. The morphology of the gold nanoseeds and Dox@TPAu was characterized using a transmission electron microscopy (TEM) system (Thermo Fisher).

Photothermal Efficiency Analysis

To measure the elevated temperature upon the photothermal conversion of Dox@TPAu at different concentrations, Dox@TPA dispersions (C_{Au} = 12.5, 25, 50, and 100 μg/mL) were subjected to NIR laser irradiation at a density of 1 W/cm^2 for 5 min, with temperature changes recorded every 0.5 min. Equal amounts of PBS irradiated with the same laser were used as a negative control. Dox@TPA dispersions (C_{Au} = 10 μg/mL) were subjected to NIR irradiation at a density of 1 W/cm^2 for 5 min and cooled to room temperature for another 5-min laser irradiation. The irradiation and cooling cycles were repeated three times, with temperature measurements recorded after each cycle.

Mitochondrial Uptake and Targeting Evaluation

BxPC-3 cells were inoculated in confocal dishes at 1×10^4 cells per dish and cultured overnight at 37°C with 5% CO_2. Dox-loaded gold nanosystems, HBAu and TPAu, were added to the cells and cultured for another 2 or 6 h, respectively. After washing thrice with PBS, the BxPC-3 cells were stained with Hoechst 33342 for 30 min and MitoTracker@Red for 30 min (E_x/E_m = 358/517 nm for Hoechst 33342, E_x/E_m = 490/550 nm for Dox, E_x/E_m = 579/599 nm for MitoTracker@Red), and then washed with PBS three times. Next, they were examined using a confocal laser scanning microscope (TCS SP5; Leica, Germany).

Measurement of Mitochondrial Membrane Potential

Mitochondrial membrane potential ($\Delta\psi m$) changes of the BxPC-3 cells were evaluated using the JC-1 assay kit. Specifically, the BxPC-3 cells were inoculated in petri dishes (1×10^5 cells per dish); cultured overnight at 37°C with 5% CO_2; and then incubated with RPMI-1640 serum-free medium, Dox, HBAu plus 808-nm laser irradiation, Dox@HBAu, Dox@TPAu, and Dox@TPAu plus 808-nm laser irradiation. The BxPC-3 cells were sequentially irradiated with NIR laser (1 W/cm^2 for 5 min) after another 3 h of incubation, and JC-1 working solution was added to the dishes and stained at 37°C for 20 min in the dark. Finally, the BxPC-3 cells were washed and analyzed using flow cytometry (FACSVerse, BD, Germany).

Cytotoxicity Analysis

The cytotoxicity of Dox, HBAu, Dox@HBAu, and Dox@TPAu on pancreatic cancer cells was measured using MTT assay. Briefly, BxPC-3 cells with apparent logarithmic growth phase were grown in 96-well plates (4×10^4 cells per well) and incubated overnight in a humidified atmosphere with 5% CO_2 at 37°C, and then incubated with various concentrations of Dox, HBAu, Dox@HBAu, and Dox@TPAu (0.5, 1, 2.5, 5, and 10 μg/mL equivalents) with or without 808-nm laser irradiation. The BxPC-3 cells were then sequentially irradiated with an 808-nm laser (1 W/cm^2 for 5 min) after 3 h of incubation, and incubated at 37°C for another 48 h.

BxPC-3 cells with apparent logarithmic growth phase were grown in 96-well plates; incubated overnight in a humidified atmosphere with 5% CO_2 at 37°C; and then treated with RPMI-1640 complete medium, Dox, HBAu plus 808-nm laser irradiation, Dox@HBAu, Dox@TPAu, and Dox@TPAu plus 808-nm laser irradiation. After 3 h of incubation, the BxPC-3 cells were sequentially irradiated with an 808-nm laser (1 W/cm^2 for 5 min) and incubated for an additional 48 h. The BxPC-3 cells were washed thrice with PBS, stained with Calcein-AM and propidium iodide (PI), kept away from light for 30 min, and then imaged using a fluorescence microscope.

Analysis of Dox@TPAu Biodistribution and Tumor Targeting

To evaluate the biodistribution and tumor targeting of Dox@TPAu, a BxPC-3 xenograft tumor model was established through subcutaneous injection of *BALB/c* athymic nude mice (male, 18–22 g, 6–8 weeks old) with BxPC-3 cell suspension. When the tumor volume reached approximately 200 mm^3, the BxPC-3 tumor-bearing mice were randomly

divided into three groups and administered Dox, Dox@HBAu, or Dox@TPAu (with a Dox-equivalent dose of 3 mg/kg) intravenously through the tail vein. The mice were sacrificed, and their main tissues were collected at 1, 3, 6, 9, and 12 h (n = 3) post injection and stored at –80°C until analysis.

The collected tissue samples were weighed, diced into small pieces, and homogenized in three volumes of ice-cold PBS. Subsequently, 50 μL of tissue homogenate was spiked with 5 μL of epirubicin (internal standard solution), mixed by vortexing with 150 μL of ethanol (chromatographic grade) for 10 min, and centrifuged at 13,000 × *g* for 20 min at 4°C to precipitate proteins. The resultant supernatants (10 μL) were measured using HPLC–MS/MS.

Anti-Tumor Efficacy Study

The BxPC-3 xenograft tumor-bearing male *BALB/c* athymic nude mice were randomly assigned to the following five groups (n = 4): PBS, Dox, Dox@HBAu, Dox@TPAu, and Dox@TPAu plus 808-nm laser irradiation. The specified formulations (with a Dox-equivalent dose of 3 mg/kg) were injected into the mice through the tail vein every 2 d seven times. For the laser irradiation groups, an 808-nm laser was used 24 h post-injection (1 W/cm^2 for 5 min). The body weight and tumor volume of mice were monitored every 2 d for 2 weeks. At the end of treatment, the mice were sacrificed, and the tumor tissues were collected and imaged. To evaluate the toxic adverse effects of these specified formulations comprehensively, major organs, including the liver, heart, spleen, lungs, and kidneys, were collected and analyzed using hematoxylin and eosin staining. To further analyze the stromal depletion ability and antitumor mechanism, tumor slices were subjected to immunohistochemistry (CD34 to assess tumor vascular density) and immunofluorescence staining (fibroblast activation protein (FAP) and α-smooth muscle actin (α-SMA) to assess CAFs).

Statistics Analysis

All experiments were performed a minimum of three times, with results reported as mean ± SD. Statistical analyses and graphing were conducted using GraphPad Prism 8 Software (San Diego, USA). A two-tailed Student's *t*-test was utilized for all analyses, and significance levels are indicated as follows: $*P < 0.05$ and $**P < 0.01$.

Results and Discussion

In this study, we utilized polydopamine to regulate crystal growth during the reduction process of gold precursors, successfully synthesizing hyperbranched virus-like gold nanoparticles (HBAu).[36] As a first step, transmission electron microscopy (TEM) was employed to characterize the gold nanoseeds, which displayed a uniform particle size—a critical factor for the synthesis of multi-level branching HBAu (Figure 1A).[37,38] As shown in Figure 1B, the gold nanoseeds exhibited a prominent absorption peak at 527 nm in the UV-Vis absorption spectrum. The gold nanoseeds were then mixed with a Tris-HCl buffer solution, followed by the sequential addition of polydopamine and tetrachloroauric acid for further seed-grafting growth to obtain the final 3D branched virus-like HBAu. HBAu with closely arranged, highly branched structures often exhibit a broadband localized surface plasmon resonance (LSPR).[39,40] UV-Vis spectroscopy indicated that broadband absorption appeared at a concentration of 12.5 μg/mL HBAu, with a linear concentration-dependent relationship observed across the measured range (Figure 1C). To enhance mitochondrial targeting, TPP-modified TPP-PEG2000-SH was coated onto the surface of HBAu via gold-thiol covalent bonds. Characterization revealed the zeta potential and average size of TPAu to be 6.59 ± 1.46 mV and 48.25 ± 4.02 nm, respectively. Moreover, the drug loading rate is 13.68 ± 2.54 mg/g, while the encapsulation rate is 31.16 ± 1.24%. (Table 1). Dox was loaded with cholesterol using its multi-level branched structure. DLS analysis revealed that the average nanoparticle size and zeta potential of Dox@TPAu were 51.94 ± 3.85 nm and –28.57 ± 1.24 mV (polydispersity index = 0.128), respectively, to improve tumor cell uptake and reduce reticuloendothelial system sequestration.[41,42] Morphological characterization confirmed that Dox@TPAu had a 3D branched virus-like morphology, which correlated with its favorable LSPR and photothermal conversion efficiency, consistent with TEM images of the microstructural features (Figure 1D–F).[43]

HBAu exhibited broad absorption across the visible to NIR range, even at low concentrations, showing high photothermal conversion efficiency concordant with our hypothesis (Figure 1C).[44] We adopted the common NIR threshold of 808 nm to evaluate the photothermal properties of HBAu, based on the skin threshold established by the

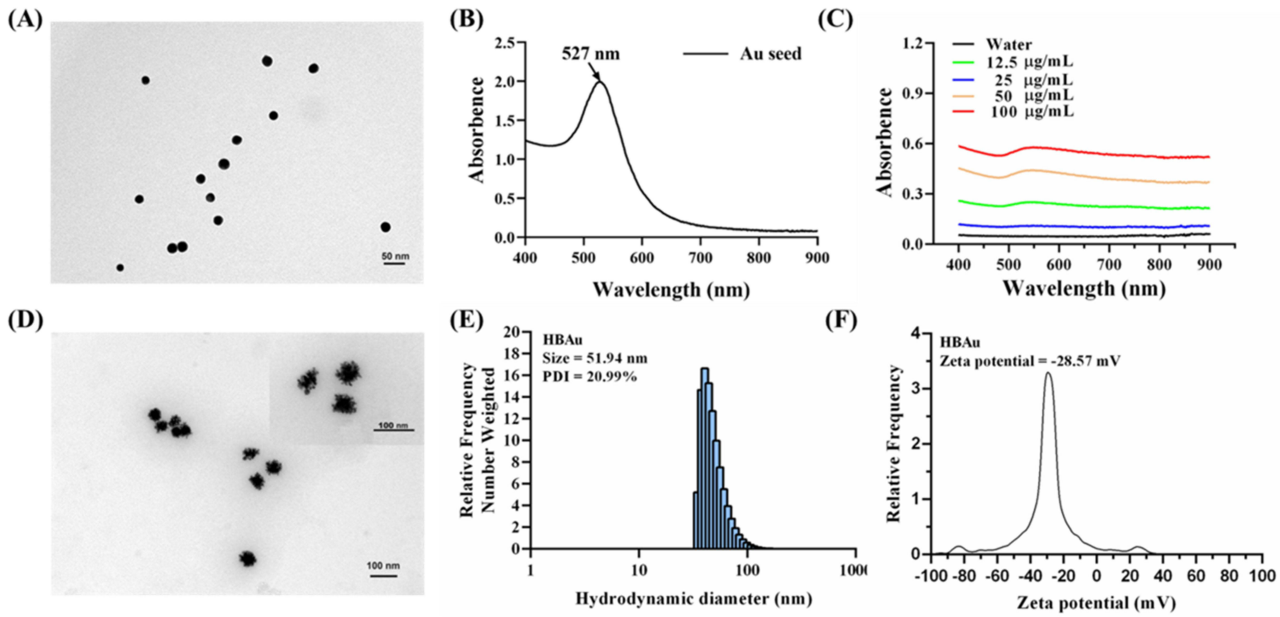

Figure 1 Preparation and characterization of Dox@TPAu. Transmission electron microscopy (TEM) images of (**A**) gold nanoseed (Scale bar, 50 nm) and (**D**) Dox@TPAu (Scale bar, 100 nm). UV-vis spectra of (**B**) gold nanoseed and (**C**) HBAu at concentrations of 0, 12.5, 25, 50, and 100 μg/mL (**E**) Size distribution and (**F**) zeta potential of Dox@TPAu.

American National Standards Institute (ANSI Z136.1–2007). This study indicated that HBAu achieved a high photothermal conversion efficiency of up to 91.0% at 808 nm (Figure S1). To investigate the photothermal conversion capabilities of Dox@TPAu comprehensively, aqueous solutions with varying concentrations of Dox@TPAu were exposed to 808-nm NIR laser irradiation at a power density of 1 W/cm^2 for 5 min, and the resulting temperature changes were monitored. The photothermal conversion efficiency of Dox@TPAu demonstrated favorable dose dependency, and the temperature of the low-concentration Dox@TPAu (12.5 μg/mL) increased from 25.0°C to 44.5°C after 5 min of 808-nm laser irradiation, prompting the deformation of 3D branched AuNPs and subsequent drug release, thereby leading to selective, sustained, and controlled in situ Dox release (Figure 2A). To further evaluate the photothermal properties of Dox@TPAu, we investigated its photothermal stability through temperature changes over three NIR irradiation cycles (Figure 2B). The results showed that the highest temperature and heating rate were nearly identical in every cycle, rather than following a marked trend, signifying the high photothermal stability of Dox@TPAu.

Mitochondria-targeted therapy strategies are widely considered effective for improving the efficacy of PTT and combination therapies because mitochondria play a crucial role in regulating tumor cell metabolism and apoptosis and are particularly susceptible to hyperthermia and oxidative damage.[45,46] Gold nanocarriers are known for their excellent LSPR and PTT; however, their limited specific targeting effects hinder their application prospects and clinical translation.[47] In this study, we used HBAu to construct Dox@TPAu, which possessed mitochondria-targeted and light-responsive drug release properties and demonstrated excellent mitochondrial targeting and hyperthermia abilities.[48] To validate this hypothesis, BxPC-3 cells were cultured with Dox-loaded HBAu and TPAu for 2 and 6 h, respectively. After

Table 1 Nanoparticle Size, Zeta Potential, PDI, EE, and DL of Gold Nanoparticles

Samples	Size (nm)	Zeta (mV)	PDI	EE (%)	DL (mg/g)
HBAu	46.73 ± 2.13	− 28.57 ± 1.24	0.097		
TPAu	48.25 ± 4.02	+ 6.59 ± 1.46	0.141		
Dox@TPAu	51.94 ± 3.85	− 18.57 ± 1.24	0.128	31.16 ± 1.24	13.68 ± 2.54

Note: Data are presented as mean ± SD (n=3).

https://doi.org/10.2147/IJN.S497346

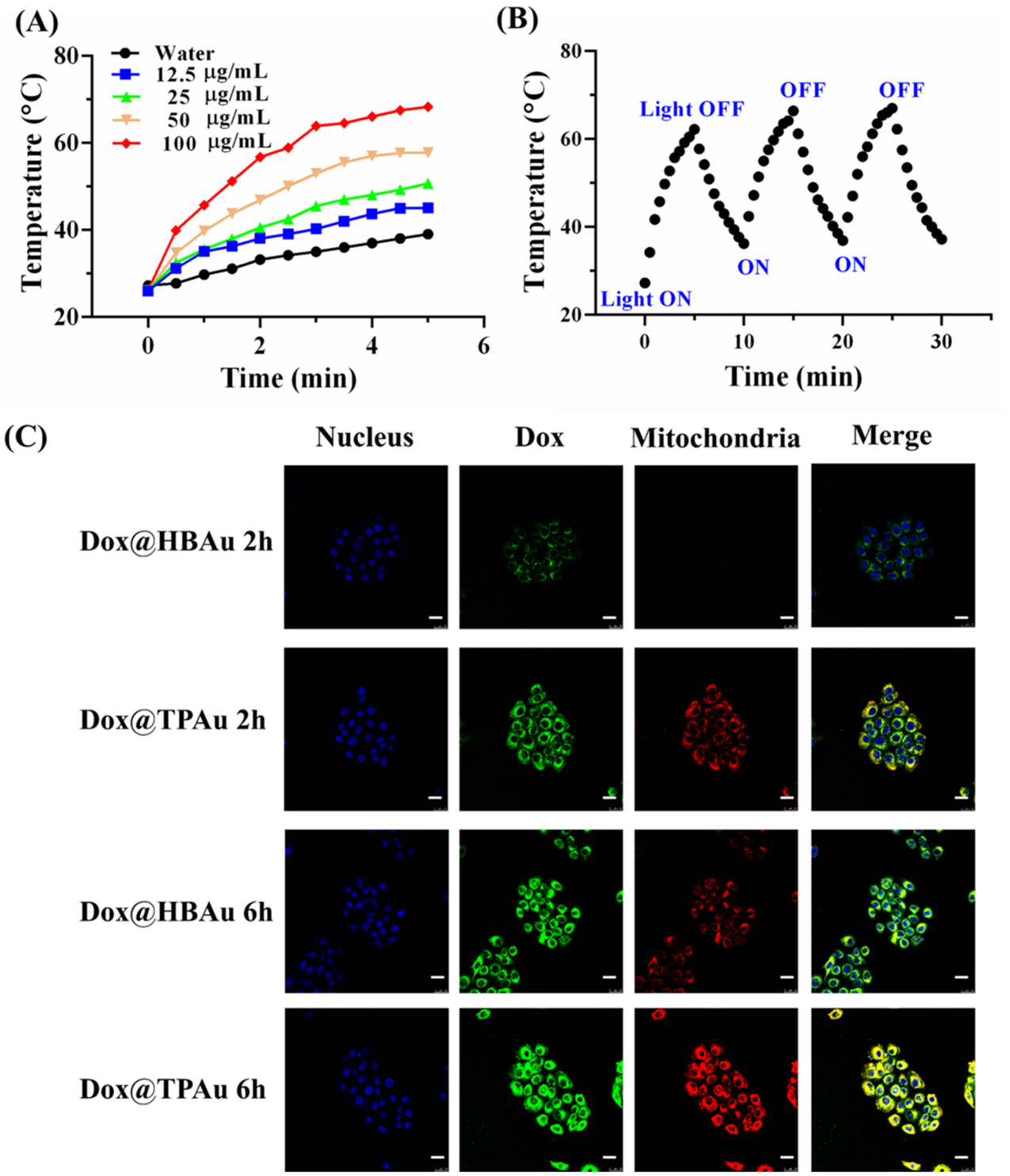

Figure 2 Photothermal properties and mitochondrial targeting of Dox@TPAu (**A**) Evaluation of photothermal effect of Dox@TPAu. The Dox@TPAu suspension (containing HBAu 0, 12.5, 25, 50, and 100 μg/mL) was exposed to an 808-nm laser (1 W/cm^2 for 5 min), and the temperature was monitored at an interval of 30s for 5 min. (**B**) Assessment of photothermal stability of Dox@TPAu through three cycles of laser on/off (**C**) Investigation of mitochondrial specificity of Dox@HBAu and Dox@TPAu. BxPC-3 cells were treated with Dox-loaded gold nanosystem (HBAu or TPAu) for 2 h or 6 h, followed by staining and imaging with MitoTracker@Red and Hoechst 33342 (Scale bar: 25 μm).

an additional 30 min of incubation, the cells were labelled with MitoTracker@Red and Hoechst 33342, red and blue fluorescent dyes that selectively stain the mitochondria and nuclei, respectively. As shown in Figure 2C, we investigated the overall effect of Dox on the cancer cell uptake of Dox@HBAu and Dox@TPAu. Enhanced spatiotemporal overlap

between the green fluorescence signal of Dox-loaded TPAu and red fluorescence signal of the mitochondrial marker was observed, leading to a pronounced superimposed yellow fluorescence within the mitochondria compared to Dox-loaded HBAu. These results confirm that Dox@TPAu possesses the ability to selectively target and accumulate within mitochondria, which can promote synergistic chemo-photothermal therapeutic effects in pancreatic cancer.

Mitochondrial abnormalities not only contribute to the metabolic reprogramming of pancreatic cancer cells but also promote tumorigenesis and the acquisition of aggressive phenotypes.[49] Therefore, we used the mitochondrial membrane-permeable dye JC-1, a mitochondrial membrane potential indicator, to monitor whether Dox, Dox@HBAu, and Dox@TPAu, with/without irradiation, induced programmed cell death and to assess the mitochondrial health of BxPC-3 cells. As depicted in Figure 3A–F, more than 90% of JC-1 aggregated in the mitochondrial matrix of the PBS control group, indicating the presence of healthy mitochondria. In addition, all other groups exhibited significantly increased proportion of JC-1 monomers within the cell population, suggesting varying degrees of mitochondrial membrane potential depolarization, which serves as an early apoptotic signal in pancreatic cancer cells. HBAu under 808-nm

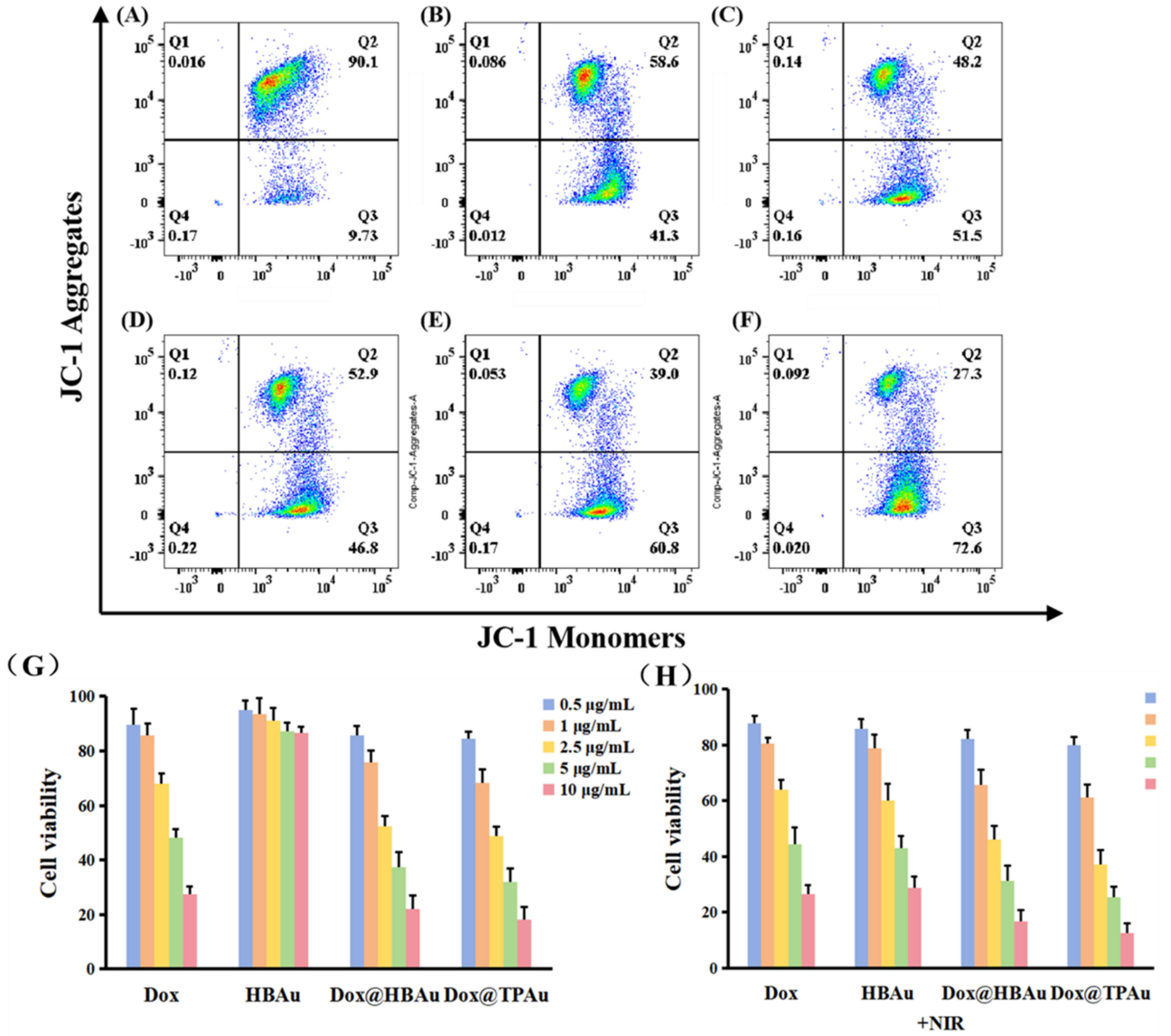

Figure 3 In vitro cytotoxicity assessment of Dox, Dox@HBAu, and Dox@TPAu on BxPC-3 cells. FACS analysis of mitochondrial dysfunction markers (JC-1, mitochondrial potential) in BxPC-3 cells following treatment with (**A**) PBS, (**B**) Dox, (**C**) HBAu plus 808-nm laser, (**D**) Dox@HBAu, (**E**) Dox@TPAu and (**F**) Dox@TPAu plus 808-nm laser (1 W/cm^2 for 5 min) (G and H) Evaluation of cytotoxic effects of various concentrations of Dox, HBAu, Dox@HBAu, and Dox@TPAu with/without irradiation on BxpC-3 cells for 48 h, with cell viability determined using the MTT assay. Data are presented as mean ± SD (n=5).

https://doi.org/10.2147/IJN.S497346

laser irradiation (1 W/cm^2 for 5 min) exhibited a similar potential as Dox to induce mitochondrial dysfunction, confirming its favorable hyperthermia therapeutic potential. Compared to Dox, Dox@HBAu, Dox@TPAu, and Dox@TPAu (which had the highest mitochondrial targetability) caused significantly high degree of mitochondrial damage, inhibited proliferation, and enhanced the apoptosis of cancer cells. In addition, Dox@TPAu with 808-nm laser irradiation exerted 1.55-fold higher cytotoxicity than Dox@HBAu, implying that mitochondrial-targeted accumulation, photo-triggerable hyperthermia therapeutic, and Dox release could significantly change the MPP and disrupt mitochondrial function in cancer cells.[50]

Chemotherapy, PTT, and synergistic therapy with or without mitochondria-targeting HBAu were preliminarily evaluated and compared in vitro. BxPC-3 cells were exposed to Dox, HBAu, Dox@HBAu, or Dox@TPAu for 48 h; the outcomes are depicted in Figure 3G and H. In the absence of irradiation, the cell survival rates of both HBAu and control groups exceeded 85% within the observed concentration range, indicating favorable biocompatibility. The survival rates of BxPC-3 cells treated with Dox, Dox@HBAu, and Dox@TPAu exhibited a significant dose-dependent relationship, with IC_{50} values of 3.67, 2.55, and 2.26 μg/mL, respectively. These findings suggest that Dox@TPAu exerted the most potent cytotoxic effect, which may be attributed to its improved accumulation via mitochondria-targeted delivery, thus promoting chemotherapy-induced cell death. In contrast, the HBAu, Dox@HBAu, and Dox@TPAu groups under 808-nm laser irradiation exhibited significantly higher cytotoxicity than the non-irradiated group, showing a significant positive correlation with an increase in HBAu content. Specifically, under 808-nm laser irradiation, Dox@TPAu (IC_{50} = 1.38 μg/mL) resulted in 3.65- and 1.48-fold higher cytotoxicity than Dox and Dox@HBAu, respectively. Furthermore, the cytotoxicity of Dox@TPAu treated with or without NIR laser irradiation was significantly inferior to that of Dox@HBAu. Therefore, the mitochondria-targeted chemo-photothermal synergistic therapy resulted in the most effective cancer cell proliferation inhibition and apoptosis-induced effects. We additionally explored the antitumor efficacy of single or combined treatments involving Dox@TPAu with mitochondrial targetability, employing the Calcein-AM/PI dual staining assay to track the levels of viable and non-viable cells. As depicted in Figure 4A, the control group exhibited a minimal percentage of non-viable cells due to regular cell turnover and maintenance processes. In contrast, both single PTT and free Dox groups demonstrated substantially higher proportions of non-viable cells, indicating their capacity to trigger apoptosis or necrosis in tumor cells effectively. When the percentages of dead cells in Dox, Dox@HBAu, and Dox@TPAu were compared, the results confirmed that virus-like HBAu could enhance the cytotoxicity of Dox by altering the cellular uptake pathway, and Dox@TPAu (possessing the mitochondria-targeting functionality) achieved the highest anti-activity. Dox@TPAu under 808-nm laser irradiation exhibited the highest PI fluorescence intensity, indicating that almost all tumor cells were eradicated, with only scattered remnants in the culture dish, resulting from the precise synergistic treatment of mitochondrial-targeted PTT and chemotherapy.

To further evaluate the biodistribution and tumor-specific targeting ability of Dox, Dox@HBAu, and Dox@TPAu following a single intravenous dose (equivalent to 3 mg/kg of Dox), a BxPC-3 cell-derived xenograft tumor model of mice was established. A validated LC-MS/MS method to track the biodistribution of the mentioned formulations was utilized.[49] The experimental mice were humanely sacrificed through cervical dislocation at 1, 3, 6, 9, and 12 h after the intravenous administration and tissues were collected. The biodistribution patterns of Dox within the specified formulations in rats are depicted in Figure 4B, C and S2. Notably, free Dox presented rapid distribution, non-targeted accumulation, and retention in rats, revealing the reasons for the severe systemic toxic adverse effects and poor quality of life in clinical patients receiving treatment. Importantly, we found that Dox@TPAu significantly improved accumulation and retention in the tumor lesions, exhibiting 1.0–2.5- and 0.2–0.6-fold higher Dox concentrations than Dox alone and Dox@HBAu, respectively. These results indicate that Dox@TPAu can significantly evade reticuloendothelial system clearance, prolong circulation, enhance tumor site-specific delivery, release Dox in a controlled manner, and improve antitumor efficacy.[51] Meanwhile, the virus-like hyperbranched TPAu accumulated in the tumor site can provide effective thermal therapy under near-infrared light stimulation, thanks to its excellent photothermal conversion efficiency.[52] Additionally, free Dox demonstrated significantly higher drug concentrations and longer retention times in the liver, kidneys, heart, and spleen compared to Dox@HBAu and Dox@TPAu. This accumulation in normal tissues can lead to severe cellular damage and tissue injury. While free Dox showed elevated concentrations within the first hour, there were

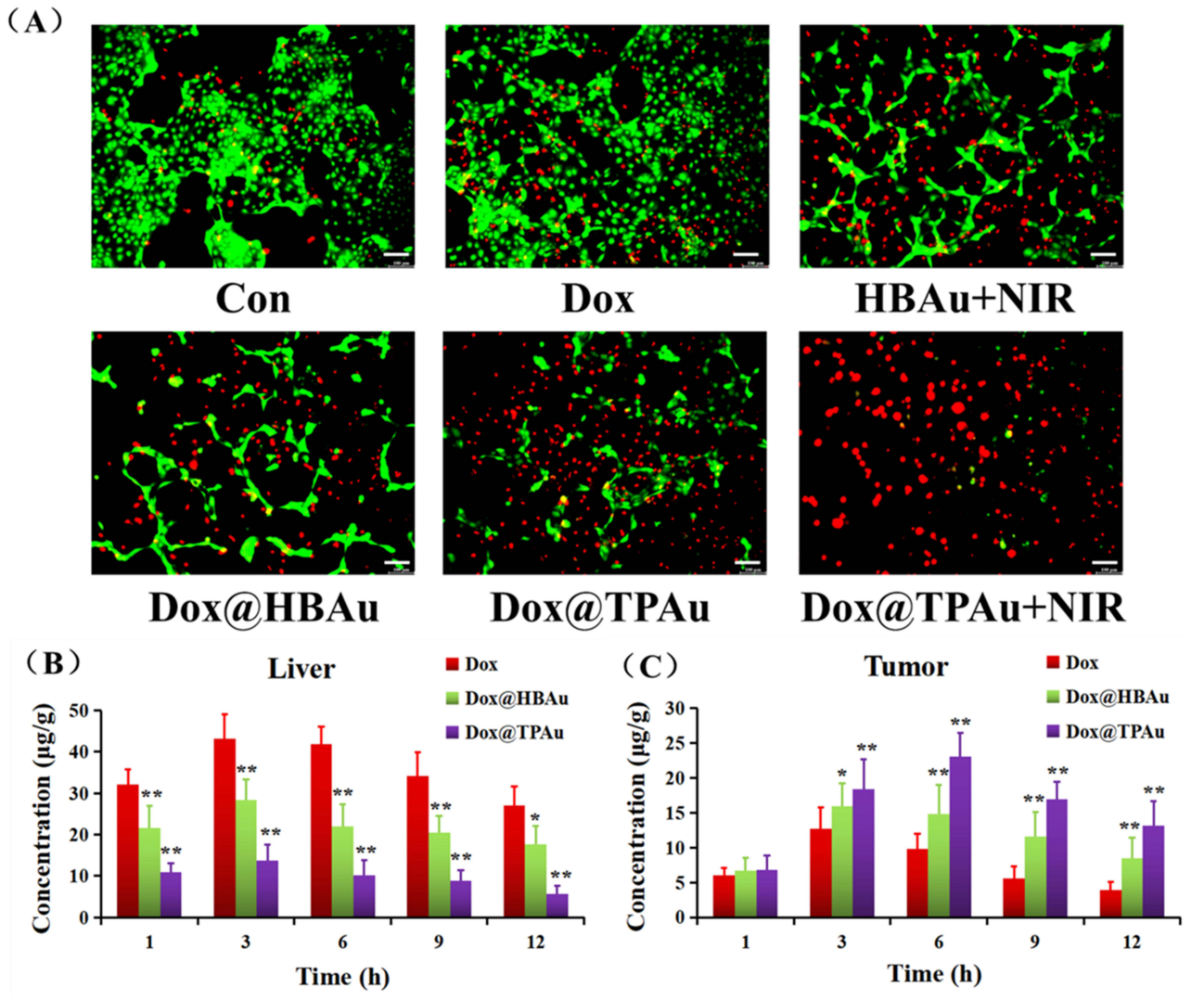

Figure 4 (**A**) Live/dead staining of BxPC-3 cells post various treatments BxPC-3 cells underwent treatment with PBS, Dox, HBAu plus 808-nm laser, Dox@HBAu, Dox@TPAu, and Dox@TPAu plus 808-nm laser (1 W/cm^2 for 5 min), followed by evaluating cell status (Scale bar: 100 μm). Biodistribution patterns of Dox in (**B**) liver and (**C**) tumor of BxPC-3 tumor-bearing mouse post intravenous administration of Dox, Dox@HBAu, Dox@TPAu at Dox dose of 3 mg/kg over different time points. Data are presented as mean ± SD (n=3), *P < 0.05 and **P < 0.01, (one-sample t-test) compared to the Dox group.

no significant differences in drug concentrations among the three formulations at later time points in the lungs. This may suggest that the branched gold nanoparticle drug delivery system does not effectively mitigate pulmonary damage.

We further assessed the antitumor efficacy of Dox@TPAu and the synergistic effects of NIR-triggered PTT combined with Dox release using a BxPC-3 cell-derived xenograft tumor mouse model. Mice were randomly divided into five groups and intravenously administered PBS, Dox, Dox@HBAu, Dox@TPAu, and Dox@TPAu under 808-nm laser irradiation (with a Dox-equivalent dose of 3 mg/kg) every 2 d for a total of seven treatments. Considering the favorable tumor distribution of Dox@TPAu at 3 h post-injection, we chose this time point for NIR irradiation (1 W/cm^2 for 5 min) at the tumor inoculation site. During the 2-week treatment period, the mouse weight and tumor volume were monitored every 2 d. As depicted in the tumor growth curve (Figure 5A), rapid malignant growth of pancreatic cancer was observed in the blank group, with the tumor volume increasing to 494.60 ± 20.85 nm within 2 weeks. Although tumor growth was inhibited in the Dox groups, the mouse weight exhibited a significant decrease, indicating that non-targeted accumulation leads to severe toxic adverse effects. Strikingly, the Dox@TPAu with 808-nm laser irradiation group displayed significantly smaller tumors than the Dox@HBAu and Dox@TPAu groups without NIR irradiation on day 14 post-inoculation. In particular, the Dox@TPAu (+NIR irradiation) group showed tumors that were only half of the initial

https://doi.org/10.2147/IJN.S497346

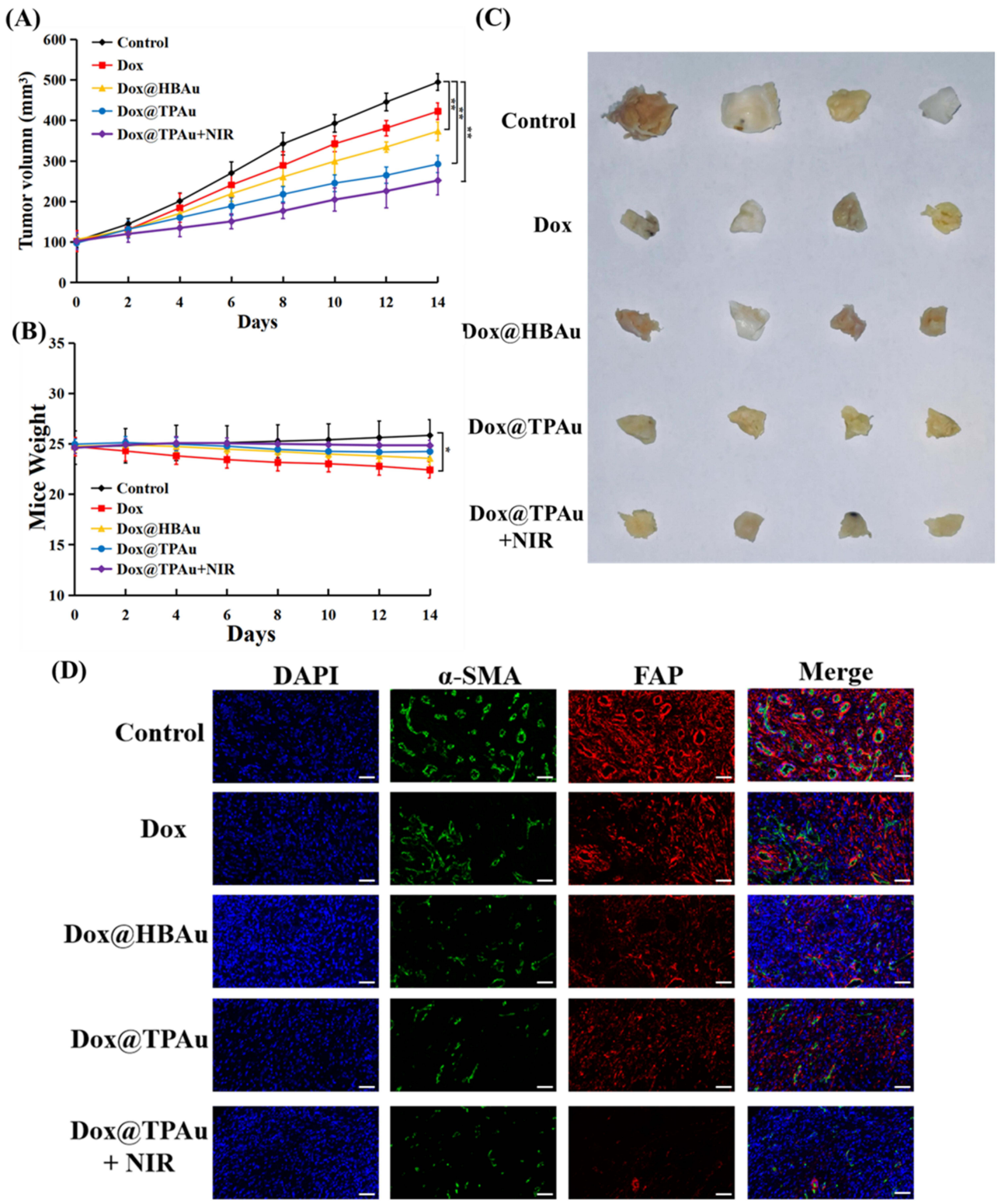

Figure 5 Investigating the synergistic therapeutic effect of Chemo-PTT with Dox@TPAu in vivo (**A**) tumor growth curves and (**B**) body weight changes of BxPC-3 tumor-bearing mice over a 2-week period post-treatment with PBS, Dox, Dox@HBAu, Dox@TPAu and Dox@TPAu plus 808-nm laser (1 W/cm^2 for 5 min) (**C**) Representative photograph of excised BxPC-3 tumors from mice treated with PBS, Dox, Dox@HBAu, Dox@TPAu, and Dox@TPAu plus 808-nm laser (1 W/cm^2 for 5 min), and tumors were collected for further analysis. (**D**) Representative immunofluorescence (IF) staining images of α-SMA and FAP positive regions in mouse tumor (Scale bar: 100 μm). Data are presented as mean ± SD (n=3), $^*P < 0.05$, and $^{**}P < 0.01$ (one-sample *t*-test) compared to the Dox group.

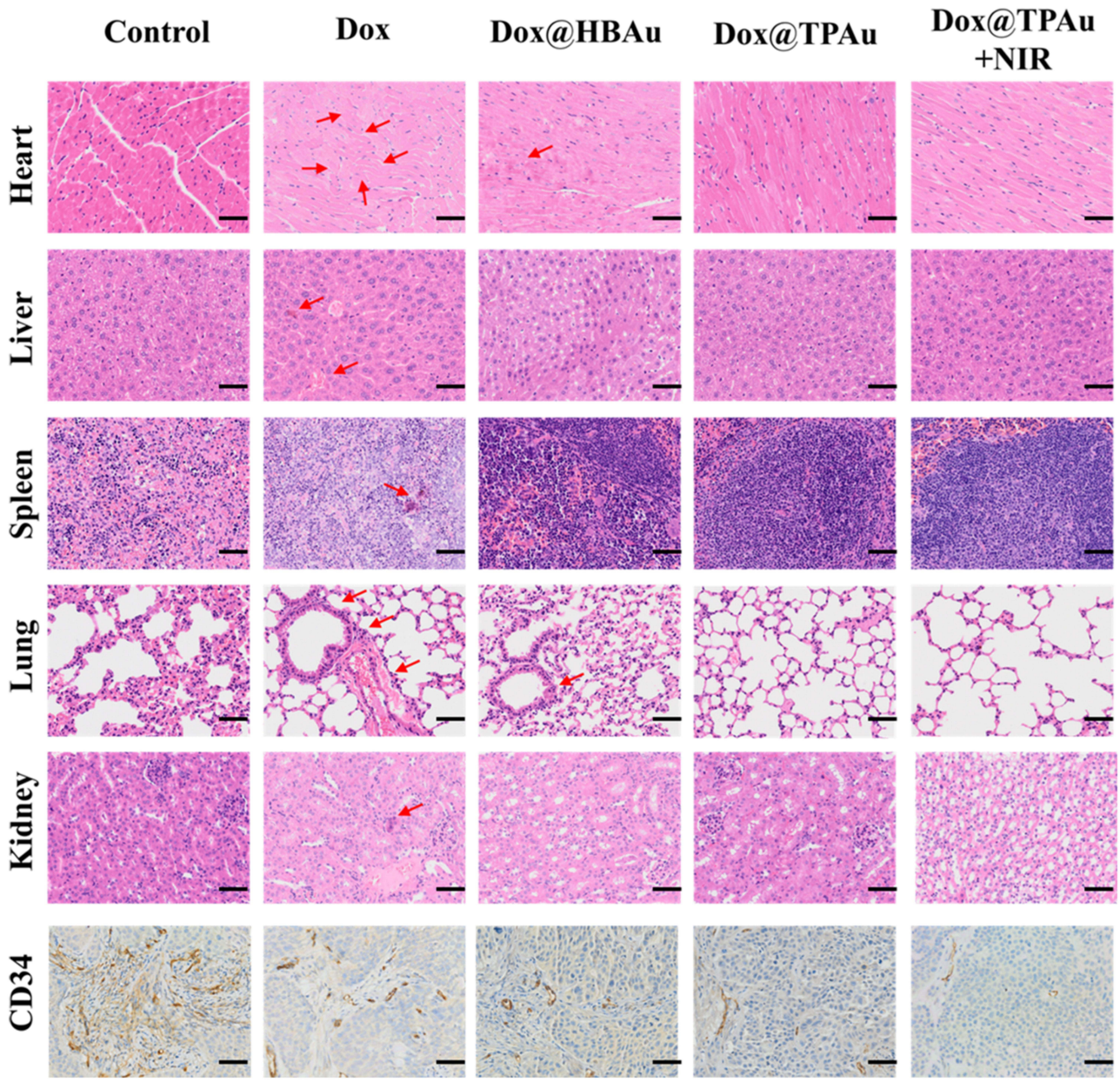

Figure 6 Representative H&E and immunohistochemical (IHC) staining images of CD34 positive areas in mouse tissues including heart, liver, spleen, lung, kidney, and tumor from BxPC-3 xenograft-bearing mouse after intravenous administration of PBS, Dox, Dox@HBAu, Dox@TPAu, and Dox@TPAu plus 808-nm laser (Scale bar: 100 μm).

tumor size, as well as those that were approximately 67.47% and 86.18% smaller than those of the Dox@HBAu and Dox@TPAu groups, respectively. More importantly, histopathological staining of major organs such as the heart, liver, spleen, lung, and kidney in the Dox@HBAu and Dox@TPAu groups did not reveal obvious damage or changes in mouse body weight, indicating that the virus-like AuNP drug delivery system can enhance tumor-targeted accumulation and reduce systemic toxicity (Figures 5B and 6).

To systematically evaluate the anti-tumor effects of Dox in the specified formulations in vivo, immunohistochemistry staining with CD34 to assess tumor vascular density and immunofluorescence staining with α-SMA and FAP to assess CAFs in pancreatic cancer xenograft mouse was conducted. As expected, the Dox@TPAu with NIR irradiation group had the lowest tumor vascular density, confirming the improved tumor microvasculature and tumor-associated angiogenesis disrupted by the virus-like gold nanoplatform through synergistic chemo-PTT.[53] Finally, we verified that the Dox@TPAu

https://doi.org/10.2147/IJN.S497346

with NIR irradiation group had a lower number of CAFs (green of α-SMA and red of FAP) than the Dox, Dox@HBAu, and Dox@TPAu groups (Figure 5C). These encouraging results indicate that the synergistic chemo-PTT significantly reduced the levels of α-SMA and FAP, which can decrease stromal desmoplasia, thereby disrupting the physical barrier for treatment and effectively delivering drugs to tumor cells. Collectively, our findings demonstrate the validity and feasibility of employing virus-like gold nanoplatforms for synergistic chemo-PTT to achieve effective stromal depletion and pancreatic cancer treatment.

Conclusions

In summary, we have developed a novel mitochondria-targeting, NIR-triggered system for the delivery of Dox that enhances PTT and enables NIR-controlled drug release. This innovative platform effectively amplifies stromal depletion and results in synergistic therapeutic effects against pancreatic cancer. The use of virus-like hyperbranched gold nanoparticles (HBAu) not only facilitated high drug-loading efficiency but also demonstrated excellent photothermal performance, achieving an efficiency of 91.0%. Characterization through UV-Vis spectroscopy, dynamic light scattering (DLS), and transmission electron microscopy (TEM) confirmed the successful synthesis of Dox@TPAu, which exhibited remarkable photo-triggered hyperthermic capabilities. This system's ability to localize within mitochondria allows for controlled drug release upon NIR irradiation, leading to significant mitochondria-dependent apoptosis and enhanced antitumor efficacy both in vitro and in vivo. Furthermore, the modification of our delivery system improved the targeting of pancreatic cancer cells and associated stromal fibroblasts, effectively enhancing drug penetration and improving treatment outcomes. While our findings illuminate the potential of this platform, several challenges remain. Continued exploration is needed to further optimize the system's targeting specificity, minimize potential off-target effects, and assess long-term safety. Future studies should focus on translational strategies, including robust preclinical trials, to pave the way for clinical applications. Overall, our platform appears to be a promising advanced strategy for pancreatic cancer treatment and is essential to the successful translation of these therapies from preclinical studies to clinical applications.

Abbreviations

α-SMA, α-smooth muscle actin; AA, l-ascorbic acid; AuNP, gold nanoparticle; CAF, cancer-associated fibroblast; DLS, dynamic laser light scattering; Dox, doxorubicin; ECM, extracellular matrix; FAP, fibroblast activation protein; HBAu, hyperbranched virus-like gold nanoparticles; ICG, indocyanine green; LSPR, localized surface plasmon resonance; NIR, near-infrared light; PBS, phosphate buffered saline; PI, propidium iodide; PTT, photothermal therapy; PVP, polyvinyl-pyrrolidone; TEM, transmission electron microscopy; TPP, triphenylphosphonium; TSC, trisodium citrate dihydrate.

Ethics Approval and Consent to Participate

All the animal experiments were approved by the Experimental Animal Center of Fujian Medical University. Animal experiments were carried out in compliance with the Guide for the Animals Care and Ethics Committee of Fujian Medical University (Certificate number: FJMU IACUC 2021-NSFC-0022). We thanks from Shiyanjia Lab (www.shiyanjia.com) for the TEM analysis. Meanwhile, we acknowledge the Fujian Medical University Ethics Committee for their kind guidance in the animal experiments and the Public Technology Service Center of Fujian Medical University.

Acknowledgments

This study is supported by the National Natural Science Foundation of China (82103689 and 32101155), Excellent Young Scholars Cultivation Project of Fujian Medical University Union Hospital (2022XH028), the National Natural Science Foundation of Fujian Province (2024J01505, 2021J01771, 2021J01346, 2020J011013 and 2022J01751), Joint Funds for the innovation of Science and Technology of Fujian province (2023Y9149), Fujian Provincial health technology project (2023GGA021). Open Research Fund of Digital Medicine Valley (2024B013).

Disclosure

The authors report no conflicts of interest in this work.

References

1. Bray F, Laversanne M, Jemal A, et al. Global cancer statistics 2022: GLOBOCAN estimates of incidence and mortality worldwide for 36 cancers in 185 countries. *CA Cancer J Clin*. 2024;74:229–263. doi:10.3322/caac.21834
2. Niu N, Shen X, Xue J, et al. Tumor cell-intrinsic epigenetic dysregulation shapes cancer-associated fibroblasts heterogeneity to metabolically support pancreatic cancer. *Cancer Cell*. 2024;42:869–884. doi:10.1016/j.ccell.2024.03.005
3. Kolbeinsson HM, Chandana S, Chung M, et al. Pancreatic cancer: a review of current treatment and novel therapies. *J Invest Surg*. 2023;36:2129884. doi:10.1080/08941939.2022.2129884
4. Grünwald BT, Devisme A, Khokha R, et al. Spatially confined sub-tumor microenvironments in pancreatic cancer. *Cell*. 2021;184:5577–5592. doi:10.1016/j.cell.2021.09.022
5. Sherman MH, Beatty GL. Tumor microenvironment in pancreatic cancer pathogenesis and therapeutic resistance. *Ann Rev Paleopathol Mech Dis*. 2023;18:123–148. doi:10.1146/annurev-pathmechdis-031621-024600
6. Qi R, Bai Y, Shi B, et al. Cancer-associated fibroblasts suppress ferroptosis and induce gemcitabine resistance in pancreatic cancer cells by secreting exosome-derived ACSL4-targeting miRNAs. *Drug Resist Updat*. 2023;68:100960. doi:10.1016/j.drup.2023.100960
7. Beatty GL, Werba G, Simeone DM, et al. The biological underpinnings of therapeutic resistance in pancreatic cancer. *Genes Dev*. 2021;35:940–962. doi:10.1101/gad.348523.121
8. Hosein AN, Brekken RA, Maitra A. Pancreatic cancer stroma: an update on therapeutic targeting strategies. *Nat Rev Gastroenterol Hepatol*. 2020;17:487–505. doi:10.1038/s41575-020-0300-1
9. Delaunay S, Pascual G, Frye M, et al. Mitochondrial RNA modifications shape metabolic plasticity in metastasis. *Nature*. 2022;607:593–603. doi:10.1038/s41586-022-04898-5
10. Wang X, Chen B, Yao H, et al. Molecular mechanism and pharmacokinetics of flavonoids in the treatment of resistant EGF receptor-mutated non-small-cell lung cancer: a narrative review. *Br J Pharmacol*. 2021;178:1388–1406. doi:10.1111/bph.15360
11. Che T, Yang X, Wu Z, et al. Mitochondria-regulated information processing nanosystem promoting immune cell communication for liver fibrosis regression. *Small*. 2024;20:2400413. doi:10.1002/smll.202400413
12. Liu Z, Sun Y, Ding S, et al. Mitochondrial transfer/transplantation: an emerging therapeutic approach for multiple diseases. *Cell Biosci*. 2022;12:66. doi:10.1186/s13578-022-00805-7
13. Zheng Z, Nan B, He Y, et al. Inhibition of histone methyltransferase PRMT5 attenuates cisplatin-induced hearing loss through the PI3K/Akt-mediated mitochondrial apoptotic pathway. *J Pharm Anal*. 2023;13:590–602. doi:10.1016/j.jpha.2023.04.014
14. Mu M, Liang X, Guo G, et al. Boosting ferroptosis and microtubule inhibition for antitumor therapy via a carrier-free supermolecule nanoreactor. *J Pharm Anal*. 2023;13:99–109. doi:10.1016/j.jpha.2022.09.003
15. Mukhopadhyay S, Encarnación-Rosado J, Kimmelman AC, et al. Autophagy supports mitochondrial metabolism through the regulation of iron homeostasis in pancreatic cancer. *Sci Adv*. 2023;9:eadf9284. doi:10.1126/sciadv.adf9284
16. Lin X, Li L, Huang Y, et al. Targeting the opening of mitochondrial permeability transition pores potentiates nanoparticle drug delivery and mitigates cancer metastasis. *Adv Sci*. 2021;8:2002834. doi:10.1002/advs.202002834
17. Mukherjee S, Bhatti GK, Bhatti JS, et al. Targeting mitochondria as a potential therapeutic strategy against chemoresistance in cancer. *Biomed Pharmacother*. 2023;160:114398. doi:10.1016/j.biopha.2023.114398
18. de Lázaro I, Mooney DJ. Obstacles and opportunities in a forward vision for cancer nanomedicine. *Nat Mater*. 2021;20:1469–1479. doi:10.1038/s41563-021-01047-7
19. Lin Q, Jing Y, Chen B, et al. Design and application of pH-responsive liposomes for site-specific delivery of cytotoxin from cobra venom. *Int J Nanomed*. 2024;19:5381–5395. doi:10.2147/ijn.s461728
20. Teng T, Lin R, Huang H, et al. Photothermal augment stromal disrupting effects for enhanced Abraxane synergy chemotherapy in pancreatic cancer PDX mode. *Biomater Sci*. 2020;8:3278–3285. doi:10.1039/d0bm00549e
21. Liu S, Pan X, Liu H. Two-dimensional nanomaterials for photothermal therapy. *Angew Chem Int Ed*. 2020;59:5890–5900. doi:10.1002/anie.201911477
22. Borlan R, Tudor M, Focsan M, et al. Dual-modal near-infrared organic nanoparticles: integrating mild hyperthermia phototherapy with fluorescence imaging. *Int J Nanomed*. 2024;19:9071–9090. doi:10.2147/ijn.s472882
23. Chen B, Zheng K, Lin X, et al. B7H3 targeting gold nanocage pH-sensitive conjugates for precise and synergistic chemo-photothermal therapy against NSCLC. *J Nanobiotechnol*. 2023;21:378. doi:10.1186/s12951-023-02078-9
24. Deepagan VG, Leiske MN, Cifuentes-Rius A, et al. Engineering fluorescent gold nanoclusters using xanthate-functionalized hydrophilic polymers: toward enhanced monodispersity and stability. *Nano Lett*. 2021;21:476–484. doi:10.1021/acs.nanolett.0c03930
25. Kim H, Baek Y, Doh J, et al. Gold nanoparticle-carrying T cells for the combined immuno-photothermal therapy. *Small*. 2023;19:e2301377. doi:10.1002/smll.202301377
26. Xu L, Wang X, Xu C, et al. Enantiomer-dependent immunological response to chiral nanoparticles. *Nature*. 2022;601:366–373. doi:10.1038/s41586-021-04243-2
27. Chen B, Wang X, Lin X, et al. Proliposomes for oral delivery of total biflavonoids extract from Selaginella doederleinii: formulation development, optimization, and in vitro–in vivo characterization. *Int J Nanomed*. 2019;14:6691–6706. doi:10.2147/ijn.s461728
28. Zhou J, Jiang Y, Duan H, et al. Compact plasmonic blackbody for cancer theranosis in the near-infrared II window. *ACS Nano*. 2018;12:2643–2651. doi:10.1021/acsnano.7b08725
29. Kabil MF, Mahmoud MY, El-Sherbiny IM, et al. Switching indication of PEGylated lipid nanocapsules-loaded with rolapitant and deferasirox against breast cancer: enhanced in-vitro and in-vivo cytotoxicity. *Life Sci*. 2022;305:120731. doi:10.1016/j.lfs.2022.120731
30. Zhong Q, Feng J, Yin Y, et al. Strain-modulated seeded growth of highly branched black au superparticles for efficient photothermal conversion. *J Am Chem Soc*. 2021;143:20513–20523. doi:10.1021/jacs.1c11242
31. Higaki T, Li Y, Jin R, et al. Atomically tailored gold nanoclusters for catalytic application. *Angew Chem Int Ed*. 2019;58:8291–8302. doi:10.1002/anie.201814156
32. Hua S, He J, Zhou M, et al. Multistage-responsive clustered nanosystem to improve tumor accumulation and penetration for photothermal/enhanced radiation synergistic therapy. *Biomaterials*. 2021;268:120590. doi:10.1016/j.biomaterials.2020.120590

33. Dong Y, Dong S, Zhao Y, et al. Mitochondria-targeting Cu(3)VS(4) nanostructure with high copper ionic mobility for photothermoelectric therapy. *Sci Adv*. 2023;9:eadi9980. doi:10.1126/sciadv.adi9980
34. Yang F, Yu W, Peng N, et al. Mitochondria-targeted nanosystem with reactive oxygen species-controlled release of CO to enhance photodynamic therapy of PCN-224 by sensitizing ferroptosis. *Small*. 2023;19:e2206124. doi:10.1002/smll.202206124
35. Feng J, Xu D, Yang F, Chen J, Wu C, Yin Y. Surface engineering and controlled ripening for seed-mediated growth of au islands on au nanocrystals. *Angew Chem Int Ed*. 2021;60:16958–16964. doi:10.1002/anie.202105856
36. Zheng YH, Cao T, Zhan QC, et al. Structurally diverse polydopamine-based nanomedicines for cancer therapy. *Acta Mater Med*. 2022;1(4):427–444. doi:10.15212/AMM-2022-0023
37. Si WD, Li YZ, Sun D, et al. Toward controlled syntheses of diphosphine-protected homochiral gold nanoclusters through precursor engineering. *ACS Nano*. 2021;15:16019–16029. doi:10.1021/acsnano.1c04421
38. Li YH, Zhao SN, Zang SQ. Programmable kernel structures of atomically precise metal nanoclusters for tailoring catalytic properties. *Exploration*. 2023;3(3):20220005. doi:10.1002/EXP.20220005
39. Fetzer F, Maier A, Scheele M, et al. Structural order enhances charge carrier transport in self-assembled Au-nanoclusters. *Nat Commun*. 2020;11(1):6188. doi:10.1038/s41467-020-19461-x
40. Su M, Han Q, Li C, et al. A supramolecular strategy to engineering a non-photobleaching and near-infrared absorbing nano-J-aggregate for efficient photothermal therapy. *ACS Nano*. 2021;15:5032–5042. doi:10.1021/acsnano.0c09993
41. Chen B, Wang X, Lin X, et al. Improved solubility, dissolution rate, and oral bioavailability of main biflavonoids from Selaginella doederleinii extract by amorphous solid dispersion. *Drug Deliv*. 2020;27:309–322. doi:10.1080/10717544.2020.1716876
42. Zhou Q, Li J, Shen Y, et al. Transcytosis-enabled active extravasation of tumor nanomedicine. *Adv Drug Deliv Rev*. 2022;189:114480. doi:10.1016/j.addr.2022.114480
43. Shi Y, van der Meel R, Lammers T, et al. The EPR effect and beyond: strategies to improve tumor targeting and cancer nanomedicine treatment efficacy. *Theranostics*. 2020;10:7921–7924. doi:10.7150/thno.49577
44. Wu P, Liu X, Liu B, et al. Recent progress in cancer therapy based on the combination of ferroptosis with photodynamic therapy. *Acta Mater Med*. 2022;1(4):1–16. doi:10.15212/AMM-2022-0025
45. Guo X, Yang N, Huang W, et al. Mito-bomb: targeting mitochondria for cancer therapy. *Adv Mater*. 2021;33:2007778. doi:10.1002/adma.202007778
46. Peng H, Yao F, Zhao J, et al. Unraveling mitochondria-targeting reactive oxygen species modulation and their implementations in cancer therapy by nanomaterials. *Exploration*. 2023;3(2):20220115. doi:10.1002/EXP.20220115
47. Liu XY, Wang JQ, Chen ZS, et al. Gold nanoparticles: synthesis, physiochemical properties and therapeutic applications in cancer. *Drug Discov Today*. 2021;26:1284–1292. doi:10.1016/j.drudis.2021.01.030
48. Zhou X, Zhou A, Chen K, et al. A responsive nanorobot modulates intracellular zinc homeostasis to amplify mitochondria-targeted phototherapy. *Small*. 2023;19:e2302952. doi:10.1002/smll.202302952
49. Wang P, Zhang T, Yang CG, et al. Aberrant human ClpP activation disturbs mitochondrial proteome homeostasis to suppress pancreatic ductal adenocarcinoma. *Cell Chem Bio*. 2022;29:1396–1408.e1398. doi:10.1016/j.chembiol.2022.07.002
50. Chen XR, Yin XL, Wang YL, et al. Organelle-specific anchored delivery system stretching a reversal of tumor hypoxia microenvironment to a combinational chemo-photothermal therapy. *Adv Funct Mater*. 2022;32:2108603. doi:10.1002/adfm.202108603
51. Chen B, Luo H, Yao H, et al. Pharmacokinetics, tissue distribution, and human serum albumin binding properties of delicaflavone, a novel anti-tumor candidate. *Front Pharmacol*. 2021;12:761884. doi:10.3389/fphar.2021.761884
52. Li J, Zheng K, Chen B, et al. Reprogramming the tumor immune microenvironment through activatable photothermal therapy and GSH depletion using liposomal gold nanocages to potentiate anti-metastatic immunotherapy. *Small*. 2024;20:e2407388. doi:10.1002/smll.202407388
53. Lei H, Pei Z, Jiang C, et al. Recent progress of metal-based nanomaterials with anti-tumor biological effects for enhanced cancer therapy. *Exploration*. 2023;3(5):20220001. doi:10.1002/EXP.20220001